Arch. Metall. Mater. **70** (2025), 1, 243-252

DOI: https://doi.org/10.24425/amm.2025.152539

D. WANG[1], Q. PANG[1*], W. LI[1], L. DU[2], G. LU[1], J. SHI[1]

STUDY ON THE INFLUENCE OF ELEMENT PARTITIONING ON THE CRYOGENIC TOUGHNESS OF INTERCRITICAL QUENCHED 9Ni STEEL

To study the promotion mechanism of the quenching, intercritical quenching, and tempering process on the cryogenic toughness of 9Ni steel, the evolution characteristics of reversed austenite in the process were investigated. The mechanism of the phase transformation of reversed austenite under the partitioning of C, Ni and Mn elements was described. The experimental results showed that the composition of Ni and Mn elements is active in the intercritical quenching process. In particular, when the content of Ni in the austenite phase increased from 9.19% to 13.46%, the volume fraction of reversed austenite increased from 3.6% to 5.6%. The interstitial C atoms formed the Snoek-Kê-Köster peak, whose activation energy increased from 1.13 eV to 1.24 eV. The element partitioning promoted the formation of reversed austenite. However, intercritical quenching can lead to an even distribution of martensitic lath bundles, with smaller length and spacing. The presence of more nucleation sites can facilitate the formation of reversed austenite. After tempering treatment, a thin film of austenite can easily form along the martensite lath, resulting in improved plasticity and toughness of 9Ni steel.

Keywords: 9Ni steel; element partitioning; internal friction; reversed austenite; intercritical quenching

1. Introduction

Liquefied Natural Gas (LNG) as a typical new clean energy has attracted worldwide attention and is increasingly being used in various fields such as people's livelihood, petrochemical industry, and transportation [1]. Due to its good strength, low temperature impact toughness, and ductility, 9 Ni steel has become the mainstream material for storage tank construction [2]. Many researchers are working to minimize energy consumption in the preparation process by reducing process steps and enhancing the efficiency of heat treatment. These efforts aim to achieve global carbon peaking and carbon neutrality as soon as possible [3].

Previous studies [4,5] have shown that the low-temperature mechanical properties of low-carbon high-Ni steels mainly depend on the formation of reversed austenite after tempering. For instance, Tavares et al. [6] demonstrated that the excellent cryogenic toughness of 9Ni steel relies on the presence of fine acicular reversed austenite achieved through quenching, intercritical quenching, and tempering (QLT) treatment. Chen et al. [7] and others emphasized the inseparable relationship between cryogenic toughness, grain refinement, and mechanical stability of retained austenite. Zhu et al. [8] analyzed and compared the fracture morphology of 9Ni steel with different thicknesses, elucidating the positive impact of Ni element on cryogenic toughness in the industrial application of LNG. This indicates that the characteristics of reversed austenite are key factors affecting the cryogenic toughness of the tested steel. However, achieving precise control over the austenite characteristics and attaining the desired microstructure design effect pose urgent technical challenges. The author's previous foundational research has demonstrated that the two-phase region ($\alpha + \gamma$) quenching treatment is an effective process for accurately controlling the morphology and volume fraction of reversed austenite [9]. This is attributed to the generation of numerous fresh martensite structures during intercritical quenching treatment. Subsequently, after tempering treatment, the new martensite grain boundaries serve as favorable nucleation sites for reversed austenite. Furthermore, this results in the largest volume fraction of reversed austenite formation, which is consistent with the conclusions reported in literature [10]. At the same time, Pan et al. [11,12] investigated the diffusion behavior of C and Ni elements at different intercritical quenching (L) temperatures. The concentration of C and Ni in the reversed austenite reached 0.4% and 18%, respectively. However, the presence of Ni and Mn elements directly influences

[1] UNIVERSITY OF SCIENCE AND TECHNOLOGY LIAONING, SCHOOL OF MATERIALS AND METALLURGY, ANSHAN LIAONING, 114051, CHINA
[2] STATE KEY LABORATORY OF METAL MATERIALS FOR MARINE EQUIPMENT AND THEIR APPLICATIONS, ANSHAN, LIAONING, 114009, CHINA

* Corresponding author: qihang25@163.com

the formation of fresh martensite and reversed austenite during the QLT process. Therefore, a comprehensive examination of the partitioning mechanism of alloying elements such as C, Ni, and Mn under different process parameters is crucial for understanding the generation of reversed austenite and for advancing the development of high-performance 9Ni steel in the future.

Based on the quenching and high temperature tempering (QT) and QLT heat treatment processes of 9Ni steel, this paper proposes using the intercritical quenching and tempering (LT) process to compare and analyze the effect of Ni and Mn element partition mechanisms on the microstructure evolution and mechanical properties of reversed austenite in 9Ni steel. Simultaneously, in response to the challenge of low and difficult detectability of the C element, an internal friction experiment is employed to investigate the partitioning of the C element in the test steel under the intercritical quenching state and its influence on the formation of reversed austenite.

2. Materials and methods

This paper utilizes the chemical composition (wt.%) of 9Ni steel, which comprises 0.05% C, 0.5% Si, 0.7% Mn, 9.15% Ni, and Fe balance. The ingot was smelted using a 200 kg vacuum induction furnace and subsequently hot forged into a billet measuring 125 mm (height)×200 mm (length)×150 mm (width). Specimens with dimensions Φ 4 mm×10 mm were cut from the billet. The phase transition points of the tested steel was determined using the DIL 805A thermal dilatometer according to standard YB T 5127-1993. The A_{c1} and A_{c3} of the tested steel were found to be 538°C and 685°C, respectively, with M_s occurring at 325°C. The 125 mm thick billet was heated to a temperature of 1250°C for 1 h, then rolling on a ϕ550 mm test mill. After undergoing 10 passes of rolling, it was transformed into a 16 mm thick steel plate. The initial rolling temperature was 1200°C, while the final rolling temperature was 1000°C. Following the final rolling, the steel plate underwent laminar water cooling treatment. Samples measuring 150 mm×80 mm×16 mm were then extracted from the surface of the rolled steel plate in the rolling direction. These samples underwent the respective QT, LT, and QLT heat treatment experiments using a box resistance furnace. The heat treatment process route is illustrated in Fig. 1.

According to GB/T228-2002, the tensile sample was cut at a standard distance of 50 mm along the rolling direction (RD) of the steel plate. The tensile test was conducted on a Zwick-Z100 universal tensile testing machine at an initial strain rate of 10^{-3} s^{-1}. Subsequently, a standard V-notch impact sample measuring 10 mm×10 mm×55 mm was cut and soaked in liquid nitrogen at –196°C. The impact test was then performed on the JBN-500 impact testing machine. To prepare the sample, a cross section perpendicular to the rolling direction (RD) was cut, ground, and mechanically polished. The samples were then etched using a 4% nitric acid alcohol etchant. The microstructure morphology of tested steel was observed using the Quanta 400HV field-emission scanning electron microscope (SEM). The fine microstructure of the tested steel was observed by taking 10 mm×10 mm×300 μm thin slices from the mother plate, thin foil specimens were also prepared by twin-jet polishing method with a 8% perchloric acid and 92% acetic acid solution, using a JEOL-2100F transmission electron microscope (TEM). The X-ray diffraction (XRD) spectra of the samples were collected using an X'pert PRO x-ray diffractometer. The measurement parameters included a Co target, a tube voltage of 35 kV, and a tube current of 40 mA. The volume fraction of reversed austenite was calculated by comparing the integrated intensities of the (211) α, (200) γ, (220) γ, and (311) γ crystal planes families. The calculation is performed using the following formula (Eq. (1) [11]):

$$V_\gamma = \frac{1}{1 + G\dfrac{I_\alpha}{I_\gamma}} \tag{1}$$

In the formula, V_γ represents the volume fraction of reversed austenite. I_α and I_γ denote the cumulative intensity of diffraction peaks corresponding to martensite and austenite in the steel, respectively. G represents the ratio of the integrated intensity factor corresponding to the FCC crystal plane $(hkl)_\gamma$ to the BCC crystal plane $(hkl)_\alpha$, where (hkl) represents the index of the corresponding crystal plane.

The sample, measuring 1 mm×2 mm×50 mm, underwent three heat treatment states. A simulation experiment was con-

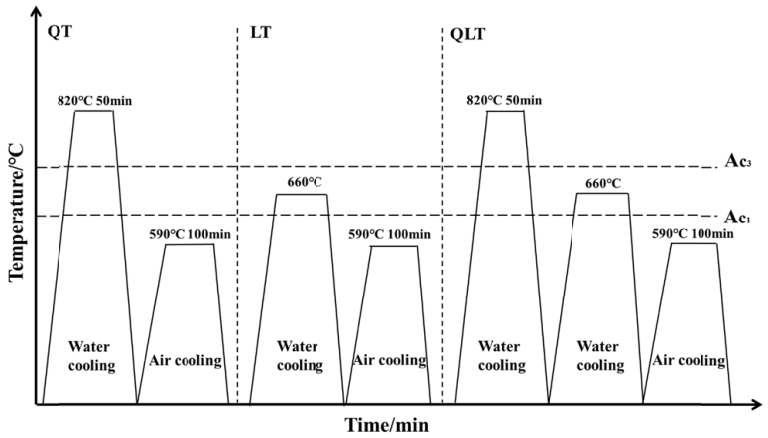

Fig. 1. Heat treatment process chart of 9Ni steel

ducted using the MFP-1000 multifunctional internal friction instrument to measure temperature, time, internal friction, and modulus during heat preservation at 660°C in the critical zone using forced vibration. The activation energy of the internal friction peak in the experimental results was calculated, and the activation energy (H) was determined using the following formula (Eq. (2) [12]):

$$H = RT_P \ln\left(\frac{k_B T_P}{hf}\right) + T_P \Delta S \tag{2}$$

In the formula, R represents the ideal gas constant. T_P (K) and f (s^{-1}) denote the temperature and frequency corresponding to the internal friction peaks, respectively. k_B refers to the Boltzmann constant, and h represents the Planck constant. ΔS represents the entropy change, with a value of 1.1×10^{-4} eV/K.

3. Results and discussion

3.1. Effect of intercritical quenching on mechanical properties of 9Ni steel

Fig. 2 represents the tensile properties of 9Ni steel at room temperature under different process conditions. As observed from the figure, the tested steel exhibits an increasing trend in both tensile strength and yield strength after undergoing QT, LT, and QLT treatments. The QLT process yields the highest tensile strength and yield strength, measuring 650 MPa and 710 MPa, respectively, indicating optimal performance in terms of strength. Comparing with the QT process, the LT and QLT processes result in an increased elongation after fracture by 27.3% and 26.8%, respectively, with similar degrees of improvement. These experimental findings align with the results reported in literature [13], suggesting that both LT and QLT processes can enhance the strength and plasticity of 9Ni steel. Further, low temperature impact tests are required to determine which process can yield the optimal comprehensive mechanical properties for the tested steel.

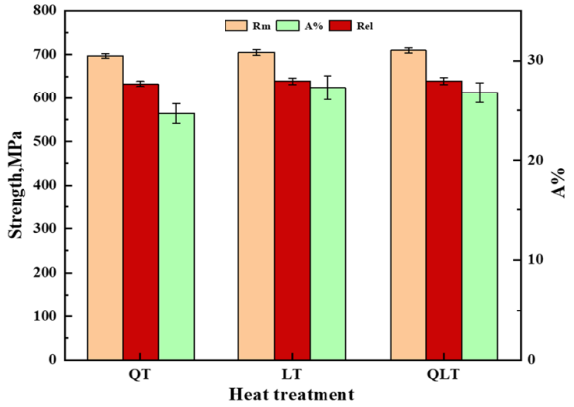

Fig. 2. Tensile properties of 9Ni steel at room temperature under different process conditions

Fig. 3 shows the relationship between the volume fraction of reversed austenite in the test steel and its low-temperature impact work under different heat treatment conditions. The corresponding

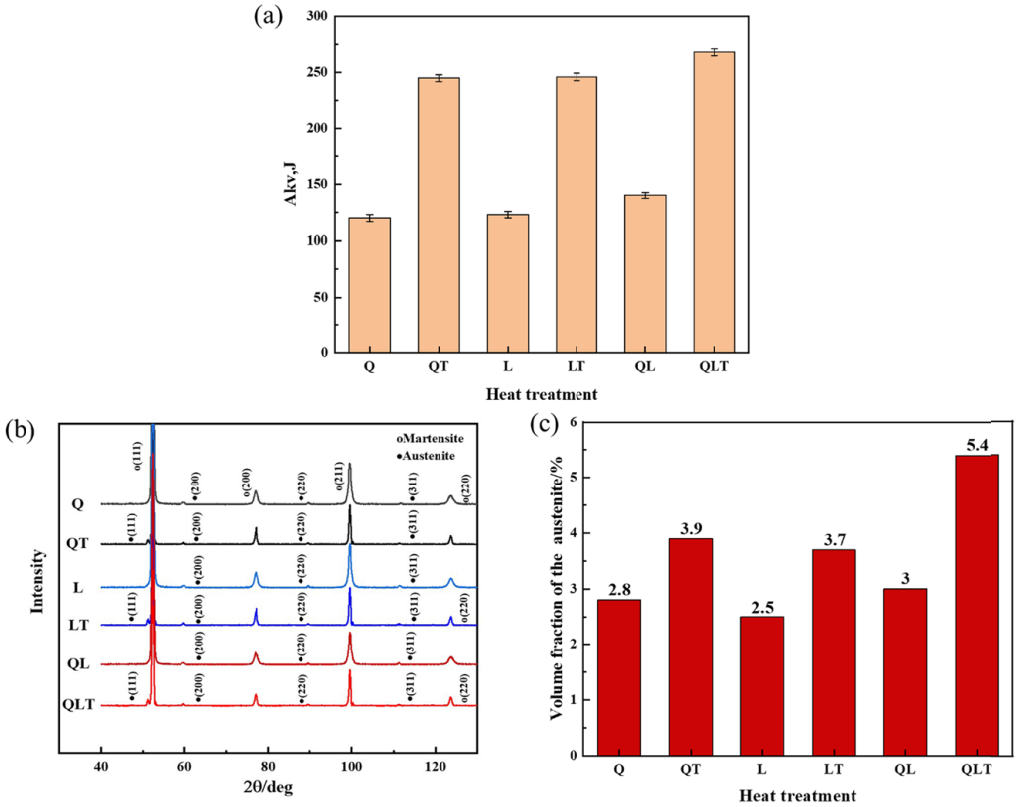

Fig. 3. Relationship between the low temperature impact energy (a), volume fractions of austenite (b), and (c) in tested steel under various heat treatment conditions

low-temperature impact energy of Q, QT, L, LT, quenching and intercritical quenching (QL) and QLT at –196°C is 120 J, 245 J, 123 J, 246 J, 140 J and 268 J, respectively.According to Fig. 3(b), after undergoing QT, LT, and QLT treatments, the volume fractions of reversed austenite in the test steel are 3.9%, 3.7%, and 5.4%, respectively. After undergoing Q, L and QL treatments, the volume fractions of retained austenite in the test steel are 2.8%, 2.5%, and 3%. Fig. 3(b) and (c) demonstrates that the test steel exhibits the best cryogenic toughness after the QLT process treatment, indicating that the volume fraction of reversed austenite directly influences its cryogenic toughness [14]. Compared with the QT and LT processes, the QLT process better ensures the volume fraction and stability of austenite in the test steel. Further exploration of the evolution mechanism of reversed austenite in steel is necessary to better understand its precise regulation.

3.2. Microstructure evolution of intercritical quenched 9Ni steel

Fig. 4 depicts the SEM microstructure of the test steel after heat treatment using the quenching (Q), L, and QL processes. As illustrated in Fig. 4(a), the test steel's microstructure is mostly made up of relatively thick lath martensite structure with a lath width of 1.8 μm and clearly visible prior austenite grain boundaries (PAGB) following Q process treatment. After L process treatment, the test steel's microstructure exhibits partial layering and slenderness, with a layer spacing of approximately 1.5 μm, as illustrated in Fig. 4(b). In Fig. 4(b), the layered structure created by martensite grows into lath bundles in different directions, and the lath bundles in different directions cross to form the illustrated interface, owing to martensite's ability to cause different grain orientations during the lamination process [15]. After the QL process, the spacing between the layers of the martensite lath is approximately 1.3 μm, and the layered structure is dense and equally dispersed, as illustrated in Fig. 4(c). It can be deduced that the L process can help refine the microstructure so that QL of the test steel produces fine fresh martensite with uniform lath size. As a result, the relationship between the change in martensite morphology and the properties of the test steel after tempering must be investigated.

Fig. 5 shows the SEM microstructure of the test steel after QT, LT, and QLT heat treatments. In Fig. 5(a), the lath spacing of the martensite structure in the test steel is approximately 2 μm. The lath structure exhibits varying degrees of destruction, and small island-like cementite appears in local areas. After LT treatment, the test steel exhibits a lath cluster structure with different orientations. The width of the lath is reduced, while the number of lath interfaces significantly increases, indicating a higher degree of interface destruction. This suggests that the average grain size of the test steel is smaller, measuring approximately 1.7 μm, as shown in Fig. 5(b). After QLT treatment, the martensite lath structure in the test steel is more evenly distributed, and the average grain size is approximately 1.3 μm, achieving the maximum refinement compared to the average grain size before tempering, as shown in Fig. 5(c). This indicates that after the tempering treatment, the lath interfaces of the three test steels exhibit varying degrees of destruction, resulting in tempered martensite and cementite [15,16]. However, the QLT process can refine the grain size to the greatest extent, providing optimal strength and toughness. In order to further understand the mechanism of the test steel's microstructure on cryogenic toughness, it is necessary to conduct further studies on the fine morphological characteristics of the reversed austenite.

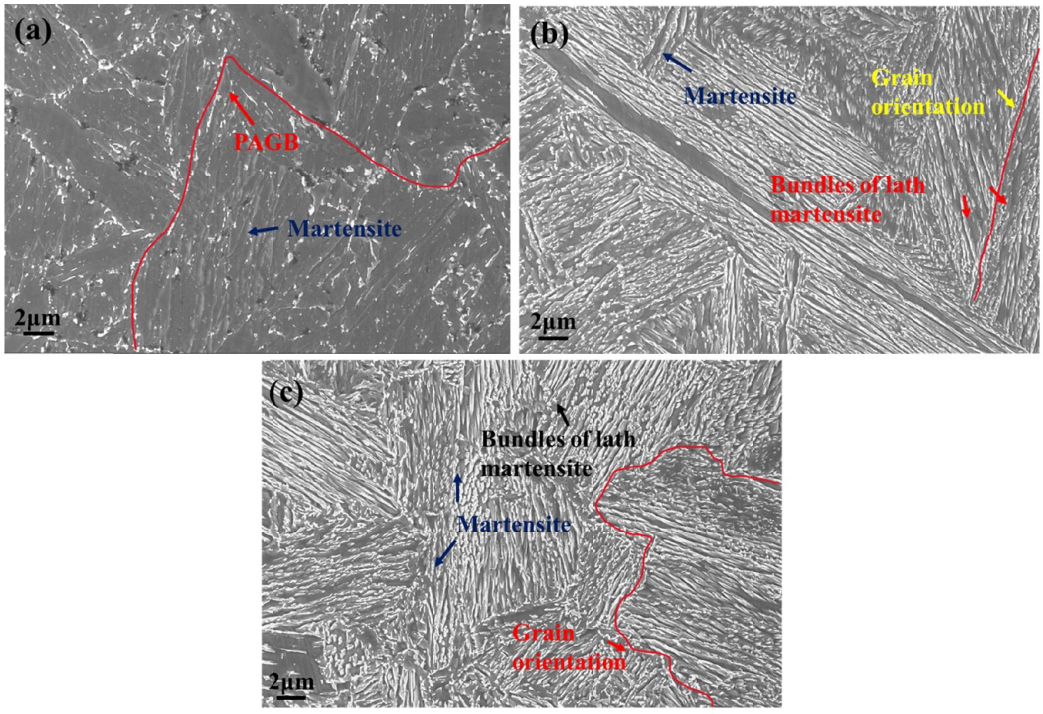

Fig. 4. SEM microstructure of 9Ni steel treated with (a) Q, (b) L, and (c) QL processes

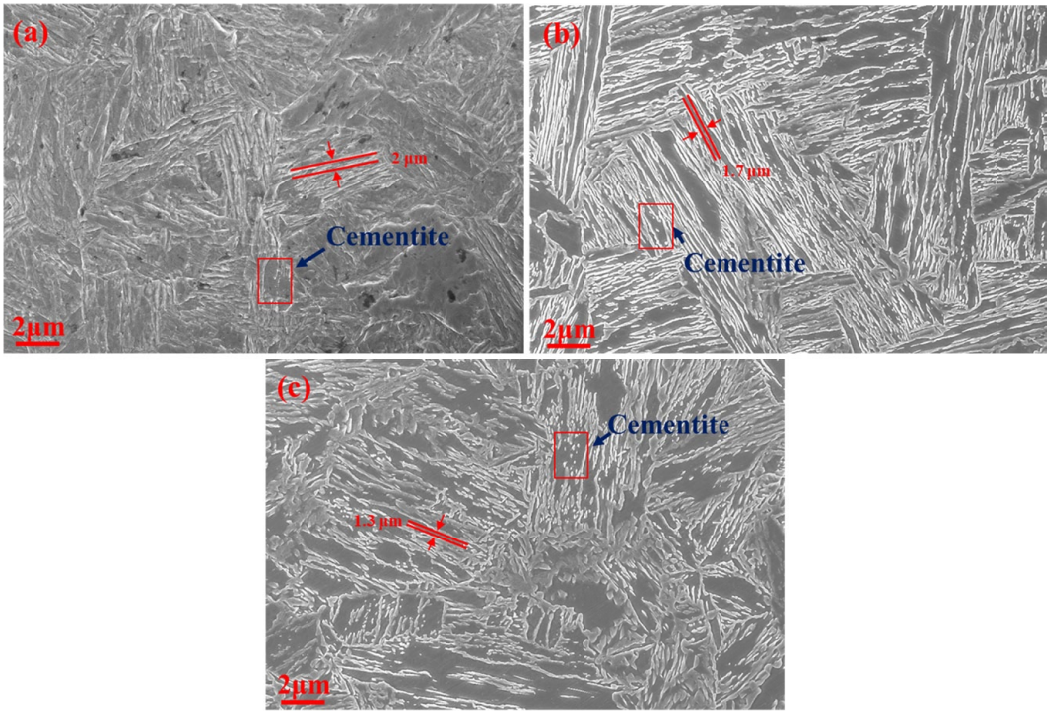

Fig. 5. SEM microstructure of 9Ni steel treated with (a) QT, (b) LT, and (c) QLT processes

3.3. Morphological characteristics of reversed austenite under different processes

Fig. 6 shows the TEM morphology of the reversed austenite and tempered martensite structures in the test steel after the QT process treatment. From the figure, it is evident that the grain boundaries of the tempered martensite are clear, and the dislocation lines within the grains are entangled, indicating their distribution characteristics as the matrix. Reversed austenite is observed along the grain boundaries of tempered martensite, and stable elements such as C, Ni, and Mn are enriched in this structure [17-19]. Through selected area electron diffraction (SAED) analysis of the lattice structures at points 1 and 2 in the TEM micrographs, it can be determined that the point 1 in Fig. 6 represents oval reversed austenite, while point 2 corresponds to tempered martensite. These findings are consistent with the results reported in the literature [8]. Similarly, in the case of the QLT process, the reversed austenite and tempered martensite are adjacent in distribution within the test steel, and a significant number of dislocation lines are present along the grain boundaries of the tempered martensite. Due to the concentrated stress and high dislocation density in the tempered martensite, atoms such as C, Ni, and Mn generate a Cottrell atmosphere, leading to the formation of enriched regions [20]. The size of these regions is approximately 300 nm, as depicted in Fig. 7. The SAED results in Fig. 7 confirm that the microstructures corresponding to points 1 and 2 represent reversed austenite and tempered martensite, respectively. According to literature [21], during intercritical quenching, a portion of the original structure in the test steel may not be fully austeni-

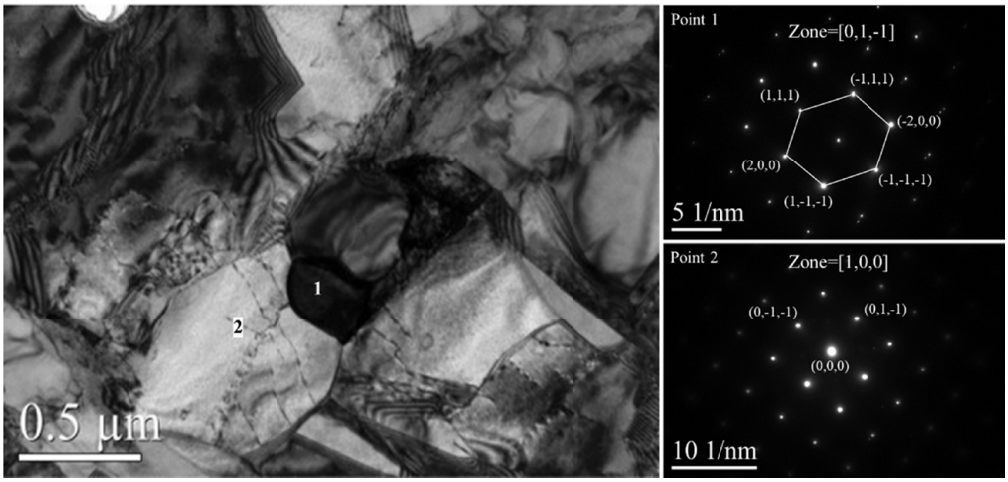

Fig. 6. TEM morphologies of reversed austenite and tempered martensite in steel samples treated with the QT process

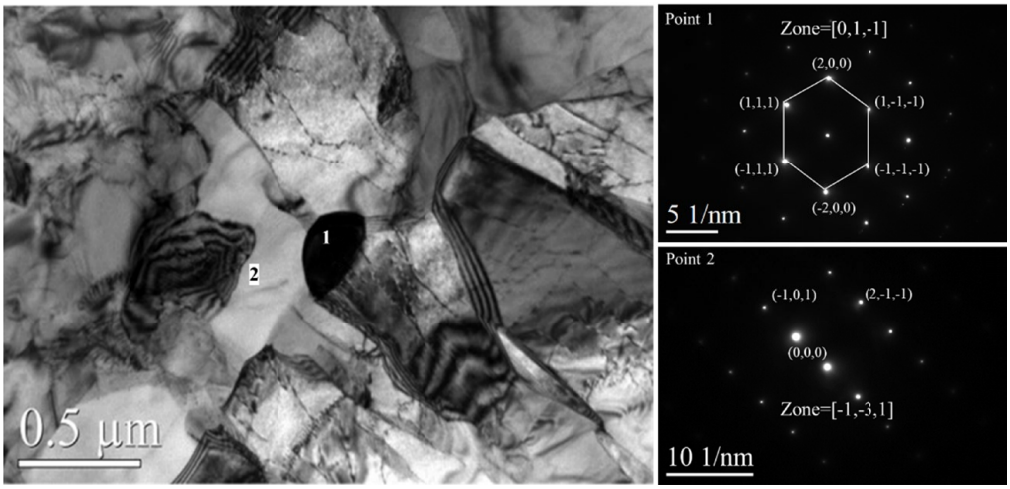

Fig. 7. TEM morphologies of reversed austenite and tempered martensite in steel samples treated with the QLT process

tized. As a result, upon cooling, thin-film retained austenite and ferrite structures are formed, primarily appearing on the boundary of the martensite lath. During the tempering process, C, Ni, and Mn atoms diffuse from the tempered martensite to the adjacent retained austenite, thereby contributing to the formation of the reversed austenite and enhancing the stability of austenite.

In summary, the element enrichment area typically occurs at the PAGB, while the reversed austenite is continuously distributed at the boundary of martensite lath bundles and the prior austenite grain boundaries, exhibiting a parallel arrangement [22], as shown in Fig. 8. During the intercritical quenching soaking at 670°C, the original martensite first undergoes martensite transformation in the region with higher energy between the plates, which becomes the nucleation site for the element enrichment region. The dislocation density in the untransformed martensitic structure sharply decreases after the intercritical quenching stage. At this point, austenite stabilizing elements such as C, Ni, and Mn in the matrix diffuse to the austenite, facilitating its recrystallization. After intercritical quenching, most of the austenite transforms into fresh martensite, while the content of C, Ni, Mn, and other elements remains high at the boundaries. A small amount of austenite is retained at room temperature, and ferrite and fresh martensite are ultimately obtained after intercritical quenching. It is necessary to analyze the influence of C, Ni, and Mn elements on the microstructure individually following intercritical quenching.

3.4. Partition mechanism of Ni and Mn elements in intercritical quenching process

Fig. 8 presents TEM and SEM images of the matrix and reversed austenite in the test steel after different processes, as well as the changes of Ni and Mn elements in reversed austenite (point 1) and tempered martensite (point 2) observed in the SEM images. As observed in the TEM image in Fig. 8(a), the bulk reversed austenite in the test steel is located at the matrix boundary after the QT process, with a large number of reversed austenite arranged in parallel. In the SEM images, the size of the block reversed austenite (point 1) is approximately 195 nm, and the peaks of Ni and Mn elements are higher compared to those of tempered martensite. Following the LT process, the austenite morphology in the test steel remains largely the same as that observed after the QT process, with a slightly smaller size of about 150 nm. The peak heights of Ni and Mn elements show slight changes, as depicted in Fig. 8(b). However, after the QLT treatment, a new thin-film morphology of reversed austenite is observed in the TEM image of the test steel, as shown in Fig. 8(b). Based on the SEM results, it can be concluded that the grain size of reversed austenite (point 1) is approximately 130 nm, with the peak height of the Ni element remaining relatively stable, while only the peak height of the Mn element exhibits changes. The EDS results reveal significant differences in the peak heights of Ni and Mn elements between the microstructures at point 1 and point 2. This indicates that the combination of Ni and Mn elements occurs among different microstructures in the test steel after heat treatment [23,24]. After the QT process, the Ni content in the reversed austenite of the test steel is 9.51%, with a small increase in Ni element observed after the LT process. However, following the QLT process treatment, the Ni element content in the test steel reaches as high as 13.46%. This suggests that, after the QLT process treatment, the Ni element content in the test steel far exceeds the average content of the matrix, and Ni atoms are enriched in the reversed austenite.

The partition rules of the Mn element in the QT, QLT, and LT processes are essentially the same as those of the Ni element. After the test steel undergoes the QT and LT processes, the Mn element in reversed austenite increases by 0.14% and 0.24%, respectively. In contrast, the Mn element content experiences a 1.4% increase after the QLT process. This indicates that under the QLT process, the diffusion of the Mn element in the austenite of the test steel is more active. Both quenching and intercritical quenching can effectively redistribute the Ni and Mn elements from the matrix to the austenite phase. However, the partitio-

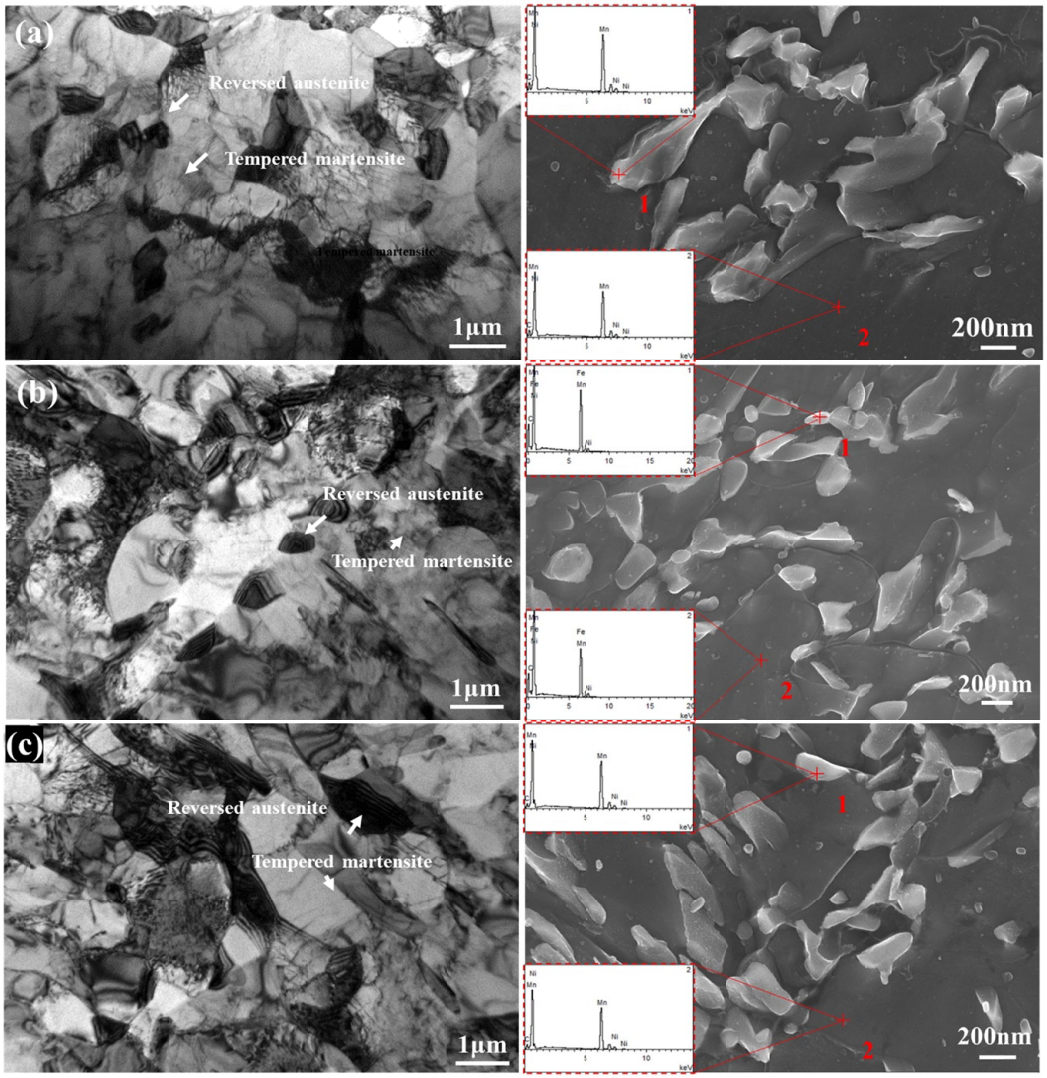

Fig. 8. SEM and TEM images of tempered martensite (matrix) and reversed austenite in different processes, along with EDS analysis of Ni and Mn elements in reversed austenite; (a) QT, (b) LT, (c) QLT

ning effect of Ni and Mn elements in the QLT process is more pronounced than that in the LT and QT processes [25], as shown in Fig. 9. Furthermore, the tempering process (low temperature partitioning), the partitioning of the C element, and its impact on reversed austenite also require further analysis.

3.5. Internal friction characterization of C element partitioning in tempering process

The measurement results of the internal friction peak and its modulus in the tested steel after the QT, QLT, and LT processes

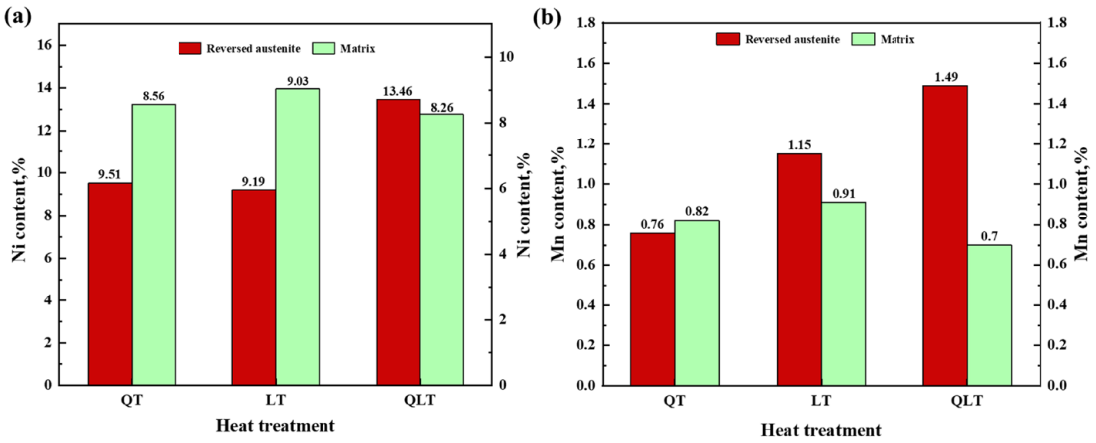

Fig. 9. Changes in Ni and Mn content in the matrix and reversed austenite with different processes

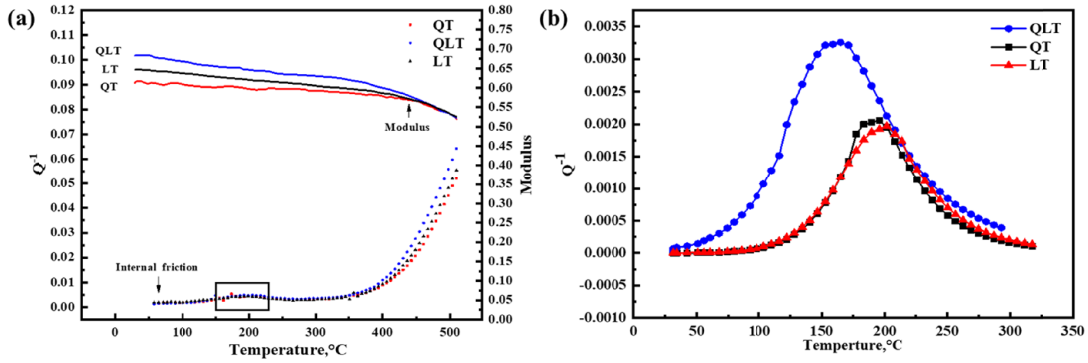

Fig. 10. The variation of internal friction and modulus (a) and the fitting curve of internal friction after heat treatment (b)

are presented in Fig. 10(a). The figure shows the appearance of a Snoek–Kê–Köster peak (SKK) in the temperature range of 150°C to 200°C during the heating process. The activation energy of the internal friction peak in the test steel, under the three heat treatment processes of QT, QLT, and LT, is H_{QT} (1.2 eV), H_{LT} (1.24 eV), and H_{QLT} (1.13 eV), respectively, as shown in TABLE 1.

TABLE 1

Shows the internal friction values and activation energy of the test steel under different processes

Heat treatment process	Peak temperature (T_P) /K	Internal friction value (Q^{-1}) /10	Activation energy (H) /eV
QT	467.42	2.06	1.20
LT	479.53	1.95	1.24
QLT	437.23	3.26	1.13

To obtain the true internal friction curve of the test steel in Fig. 10(b), the back and bottom portions of the actual measured internal friction curve were removed. The diagram shows that during the QT process, the SKK peak height of the tested steel is slightly higher than that of the LT process, while the peak width of both SKK peaks remains almost the same. Conversely, during the QLT process, both the SKK peak height increases significantly. The height of the SKK peak in the α-Fe solid solution of the tested steel, which contains a small amount of soluble carbon, is directly proportional to the concentration of the Cottrell atmosphere. This concentration, referred to as C_d, can be determined by the damping caused by dislocation drag and the presence of interstitial Cottrell atmosphere. C_d can be expressed as a function of the concentration of interstitial Cottrell atmosphere (Eq. (3) [26]):

$$C_d = C_1 e^{H_b/(RT)} \tag{3}$$

Where C_1 is the concentration of the C atom in the lattice (wt.%), H_b is the binding energy between C and the dislocation (KJ/mol), and T is the thermodynamic temperature (K).

The peak height of SKK increases as the value of C_d increases until the solute concentration of the Cottrell atmosphere in the α-Fe solid solution reaches saturation [27]. Once the Cottrell atmosphere becomes supersaturated, the solid solution C atom is deposited on the dislocation line, causing C_d to decrease. This results in a shorter length of the dislocation line and a significant decrease in the damping of SKK. Therefore, it can be inferred that the SKK peak is a characterization method used to determine the relative soluble carbon content in α-Fe solid solution.

The carbon content in the solid solution of α-Fe martensite is found to be lower in the QLT process compared to the QT and LT processes, as observed from the SKK peaks of the three heat treatment states. This observation suggests that the QLT treatment effectively reduces the carbon content in the matrix, playing a crucial role in purifying the matrix. During the tempering process, C elements are partitioned into austenite, causing A_{c1} to drop below the tempering temperature. Consequently, austenitic transformation occurs in C-rich regions. As the phase transition process continues, austenitic stable alloying elements such as Ni and Mn are enriched in the austenitic phase through short-range diffusion, resulting in the formation of reversed austenite [28]. As the peak temperature of SKK increases, the activation energy also increases, indicating the presence of higher resistance that needs to be overcome [29-31]. This increased resistance weakens the partitioning effect, making it challenging for the C element to partition during the QT and LT processes. Consequently, the formation of reversed austenite during the tempering process is reduced.

4. Conclusions

This paper presents a designed two-phase quenching (LT) process to quantitatively study the mechanism of the QLT process and improve the toughness of 9Ni steel at low temperatures. Additionally, the influence of the partitioning of C, Ni, and Mn elements on the production of reverse austenite is discussed. The study concludes with the following findings:

(1) Intercritical quenching can create stratified lath martensite in the tested steel, resulting in the formation of parallel and fine new martensite. This, in turn, improves the mechanical properties of the steel. The QLT process treatment resulted in the tested steel exhibiting the best comprehensive mechanical properties, including a yield strength of 650 MPa, tensile strength of 710 MPa, and low-temperature impact

energy of 268 J, respectively. The volume fraction of reversed austenite in the steel was 5.4%.

(2) Intercritical quenching promotes the segregation of Mn and Ni atoms towards reversed austenite. Subsequent tempering treatment effectively stabilizes this partitioning effect at high temperatures, resulting in minimal changes to the Ni and Mn content in the reversed austenite of the test steel. Following QLT treatment, the mass fractions of Ni and Mn in the austenite are approximately 13.46% (wt.%) and 1.49% (wt.%), respectively. The concentration of Ni and Mn elements leads to the reversed austenite with the highest volume fraction and high stability, which improves cryogenic toughness.

(3) The content of reversed austenite during the tempering stage, which is a low-temperature partitioning process, is influenced by the level of carbon partitioning in the tested steel. Additionally, the internal friction activation energy of the test steel increases to 119 KJ/mol after undergoing the LT treatment. Comparatively, the QLT process results in the tested steel exhibiting a higher internal friction peak than the LT process. This suggests that the QLT heat treatment process is more efficient in reducing the solid solution carbon content in the α-Fe matrix, allowing for carbon allocation to the γ-Fe phase. The resulting local carbon enrichment in the microstructure of the tested steel promotes the formation of reversed austenite.

Acknowledgment

This study was funded by the national natural Science Foundation of China (No. 52004122).

Funding and/or Conflicts of interests/Competing interests

The authors declare that there are no conflict of interests, we do not have any possible conflicts of interest in this paper.

REFERENCES

[1] W. Mu, Y. Cai, M. Wang, Effect of precipitates on the cryogenic fracture toughness of 9%Ni steel flux cored arc weld. Materials Science and Engineering A **3**, 141418 (2021).

[2] S. Khodir, T. Shibayanagi, M. Takahashi, H. Abdel-Aleem, K. Ikeuchi, Microstructural evolution and mechanical properties of high strength 3–9% Ni-steel alloys weld metals produced by electron beam welding. Materials & Design **60**, 391-400 (2014).

[3] M. Wang, Z. Liu, Effects of ultra-fast cooling after hot rolling and intercritical treatment on microstructure and cryogenic toughness of 3.5% Ni steel. Journal of Materials Engineering and Performance **26**, 3016-3024 (2017).

[4] X. Zhao, T. Pan, Q. Wang, H. Su, C.F. Yang, Q.X. Yang, Y.Q. Zhang, Effect of intercritical quenching on reversed austenite formation and cryogenic toughness in QLT-processed 9% Ni steel. Journal of Iron and Steel Research, International **14**, 240-244 (2007).

[5] H.Y. Zhao, R.P. Liu, C.J. Wang, J.X. Liang, J.Q. Hu, Influence of QLT and QT heat treatment process on properties of 9Ni steel. Heat Treatment of Metals **43**, 100-104 (2018).

[6] S.S.M. Tavares, C.R. Rodrigues, C.A.S. de Oliveira, C.B. Woyames, J. Dille, Influence of heat treatments on microstructure and toughness of 9% Ni steel. Journal of Materials Engineering and Performance **27** (4), 1530-1536 (2018).

[7] Q. Chen, W.N. Zhang, S. Tang, P.J. Wang, J. Chen, Z.Y. Liu, Microstructural heredity of Ni-containing cryogenic steel and its effect on the toughness at 77K. Materials Science and Engineering: A **832**,142441 (2022).

[8] Y.G. Zhu, W.D. Mu, Y. Cai, D.Q. Xin, M. Wang, A novel high-efficient welding technology with rotating arc assisted by laser and its application for cryogenic steels. Journal of Manufacturing Processes A2, **68** (2021).

[9] D. Wang, Q. Pang, J. Cui, et al., Effect of intercritical quenching soaking time on cryogenic toughness and internal friction characterization of 9Ni steel [J]. Mater. Res. Express **10**, 116510 (2023.

[10] H.L. Zhang, M.Y. Sun, Y.X. Liu, D.P. Ma, B. Xu, M.X. Huang, D.Z. Li, Y. Li, Ultrafine-grained dual-phase maraging steel with high strength and excellent cryogenic toughness. Acta Materialia 116878 (2021).

[11] T. Pan, J. Zhu, H. Su, C.F. Yang, Ni segregation and thermal stability of reversed austenite in a Fe–Ni alloy processed by QLT heat treatment. Rare Metals **34**, 776-782 (2015).

[12] J. Chen, Z.Y. Liu, The combination of strength and cryogenic impact toughness in low carbon 5Mn-5Ni steel. Journal of Alloys and Compounds **837** (2020).

[13] Q. Pang, C. Geng, J. Wang, W. Li, Internal friction study on the influence of pre-deformation on hydrogen embrittlement sensitivity of dual-phase steel. Archives of Metallurgy and Materials **67**, 1315 (2022).

[14] W. Hou, Q. Liu, J. Gu, Nano-sized austenite and Cu precipitates formed by using intercritical tempering plus tempering and their effect on the mechanical property in a low carbon Cu bearing 7 Ni steel. Materials Science and Engineering **780**, 139181-139189 (2020).

[15] S.J. Wu, G.J. Sun, Q.S. Ma, Q.Y. Shen, L. Xu, Influence of QLT treatment on microstructure and mechanical properties of a high nickel steel. Journal of Materials Processing Technology **213**, 120-128 (2013).

[16] E.J. Barrick, J.N. Dupont, The influence of martensitic microstructure and oxide inclusions on the toughness of simulated reheated 10 wt% Ni steel weld metal multi-pass fusion zones. Materials Science and Engineering A **801**, 140336 (2021).

[17] C.C. Kinney, K.R. Pytlewski, A.G. Khachaturyan, et al., The microstructure of lath martensite in quenched 9Ni steel [J]. Acta Materialia **69**, 372-385 (2014).

[18] J. Chen, T. Shuai, Z.Y. Liu, G.D. Wang, Microstructural characteristics with various cooling paths and the mechanism of embrittlement and toughening in low-carbon high performance bridge steel. Materials Science & Engineering A **559**, 241-249 (2013).

[19] Q.Y. Chen, J.K. Ren, Z.L. Xie, W.N. Zhang, J. Chen, Z.Y. Liu. Correlation between reversed austenite and mechanical properties in a low Ni steel treated by ultra-fast cooling, intercritical quenching and tempering. Journal of Materials Science **55**, 1840-1853 (2020).

[20] Q.Y. Chen, W.N. Zhang, Z.L. Xie, J.K. Ren, J. Chen, Z.Y. Liu, Influence of intercritical temperature on the microstructure and mechanical properties of 6.5 Pct Ni steel processed by ultra-fast cooling, intercritical quenching and tempering. Metallurgical and Materials Transactions A **51**, 3030-3041 (2020).

[21] C. Kuang, S. Zhang, J. Li, Effects of pre-strain and baking parameters on the microstructure and bake-hardening behavior of dual-phase steel. International Journal of Minerals, Metallurgy, and Materials **21**, 766 (2014).

[22] J. Hu, L. X. Du, G.S. Sun, H. Xie, R.D.K. Misra, The determining role of reversed austenite in enhancing toughness of a novel ultra-low carbon medium manganese high strength steel. Scripta Materialia **104**, 87-90 (2015).

[23] X.G. Tao, L.Z. Han, J.F. Gu, Effect of tempering on microstructure evolution and mechanical properties of X12CrMoWVNbN10-1-1 steel. Materials Science and Engineering: A **618**, 189-204 (2014).

[24] M. Wang, Z.Y. Liu, C.G. Li, Correlations of Ni contents, formation of reversed austenite and toughness for Ni-containing cryogenic steels. Acta Metallurgica Sinica (English Letters) **30**, 238-249 (2017).

[25] Z. Huang, Y. Cai, W. Mu, Y.Z. Li, X.M. Hua, Effects of laser energy allocation on weld formation of 9%Ni steel made by narrow gap laser welding filled with nickel based alloy. Journal of Laser Applications **30**, 32013 (2018).

[26] S. Chang, J. Zhang, Z. Zhu, G. Kang, L. Peng, X. Huang, The ratchetting and retained austenite transformation of medium-manganese transformation-induced plasticity steel during asymmetrical cyclic stressing. Fatigue & Fracture of Engineering Materials and Structures **6**, 45 (2022).

[27] Y. Cao, C. Luo, L. Zhao, Y. Peng, L. Song, C. Ma, Z. Tian, M. Zhong, Y. Wang, Microstructural evolution and mechanical properties of laser-welded joints of medium manganese steel. Journal of Iron and Steel Research International **27**, 13 (2020).

[28] S.D. Raducan, T.M. Davison, R. Luther, G.S. Collins, The role of asteroid strength, porosity and internal friction in impact momentum transfer. Icarus **329**, 282-295 (2019).

[29] B. Soenen, A.K. De, S. Vandeputte, B.C. De Cooman, Competition between grain boundary segregation and Cottrell atmosphere formation during static strain aging in ultra low carbon bake hardening steels. Acta Materialia **52**, 3483-3492 (2004).

[30] K. Zhang, D. Tang, H.B. Wu, Effect of Heating Rate Before Tempering on Reversed Austenite in Fe-9Ni-C Alloy. Journal of Iron and Steel Research International **9**, 6 (2012).

[31] A. Rasti, H.R. Adarmanabadi, M. Pineda, J. Reinikainen, Evaluating the effect of soil particle characterization on internal friction angle. American Journal of Engineering and Applied Sciences **14**, 129-138 (2021).